Journal of Vibration and Acoustics

Technical Briefs

Fourier Series Analysis of Epicyclic Gearbox Vibration

James McNames
Assistant Professor, Department of Electrical & Computer Engineering, Portland State University, Post Office Box 751, Portland, OR 97207-0751
e-mail: mcnames@pdx.edu.

Synchronous averaging is difficult to use with epicyclic gear systems because the dominant frequencies are slightly skewed and asymmetrical. This Tech Brief uses Fourier series analysis to add new insight to this phenomenon. The results are illustrated on vibration data recorded from a Cobra AH-1S helicopter gearbox.
[DOI: 10.1115/1.1403735]

1 Introduction

Epicyclic gears are used in many applications because they can achieve a large torque/speed ratio in a compact package. In most gearboxes, the estimated spectrum of the vibration signal is symmetric and centered at the meshing frequency. For epicyclic gears, the estimated spectrum is typically asymmetric and the dominant frequency component does not occur at the meshing frequency. This is an important observation because some of the popular methods of fault detection use the meshing frequency and sideband signal power as an indication of the gearbox health [1,2].

McFadden and Smith [3] were the first to recognize that this effect was due to the varying phase angles of the vibration produced by each of the planet gears. They used phasor sums to identify the dominant spectral components, but were unable to predict the relative amplitudes of the dominant components. This study generalizes their work using continuous-time Fourier series (CTFS) analysis. This provides a more thorough and intuitive explanation of the observed spectrum and leads to a number of insights that could not be gained with phasor sums alone.

2 Fourier Series Analysis

McFadden and Smith [3] describe a model of the gearbox vibration in which the total vibration is equal to the sum of vibrations due to each planet gear, $v(r)=\Sigma_{i=1}^{P} v_i(r)$, where P is the number of planet gears and r is the number of carrier revolutions. The vibration due to each planet gear, $v_i(r)$, is modeled as a periodic amplitude-modulated signal with a frequency equal to the meshing frequency that grows in amplitude and then decays as each planet passes the vibration sensor. Under ideal conditions, the shape of the vibration pattern is the same for each planet gear, but shifted in time. Thus, the total vibration may be written as

$$v(r)=\sum_{i=1}^{P} v_1\left(r-\frac{i-1}{P}\right), \tag{1}$$

where $v_1(r)$ is the vibration due to the first planet gear that passes the transducer at the beginning of each revolution. The vibration of the planet gears measured by a fixed sensor is modeled as $v_i(r)=w_i(r)m_i(r)$, where $w_i(r)$ represents the time-varying amplitude of the transmission path from the vibration source to the sensor due to the gearbox elasticity and $m_i(r)$ represents the vibration due to the planet meshing with the annulus. The baseband signal $w_i(r)$ is periodic with a fundamental frequency of 1 cycle per revolution (cpr). The modulating signal $m_i(r)$ is periodic with a fundamental frequency of T cpr, where T is the number of teeth on the annulus gear.

One of the surprising consequences of a Fourier series representation of the epicyclic vibration is that, under most conditions, the power spectrum at the meshing frequency (T cpr) is zero. Although the vibration of a single planet gear repeats every cycle (1 cpr), the total vibration contains P copies of this vibration equally spaced apart due to each of the planet gears. The total vibration therefore has a fundamental frequency of P cpr and the continuous-time Fourier series (CTFS) representation of the total vibration can be written as

$$v(r)=\sum_{k=-\infty}^{+\infty} \alpha_k e^{j2\pi kPr}. \tag{2}$$

Thus, the signal is only composed of frequencies that are integer multiples of P cpr. Even though each planet is generating a vibration at T cpr, the total vibration does not have any components at the meshing frequency, unless T is an integer multiple of P.

Since the ith planet gear produces a vibration that is just a delayed copy of the first planet gear, $v_i(r)=v_1(r-(i-1)/P)$, the CTFS coefficients of the ith planet gear are related to the coefficients of the first by $a_{i,k}=e^{-j2\pi((i-1)/P)k}a_{1,k}$, where the CTFS representation of the vibration due to the i^{th} planet is

$$v_i(r)=\sum_{k=-\infty}^{\infty} a_{i,k} e^{-j2\pi kr}. \tag{3}$$

Although the amplitudes of these coefficients are equal for all of the planet gears, $|a_{i,k}|=|a_{1,k}|$, the sum of the coefficients is zero, except at multiples of P. This phenomenon is due to the phase differences of the coefficients.

At integer multiples of P the phase shift of each planet's CTFS coefficient $a_{i,k}$ is a multiple of 2π and, since $e^{-j2\pi i}=1$ for any integer i, the coefficients are in phase with each other and equal. The total vibration may therefore be written as

Contributed by the Technical Committee on Vibration and Sound for publication in the JOURNAL OF VIBRATION AND ACOUSTICS. Manuscript received March 2000; revised June 2001. Associate Editor: G. W. Flowers.

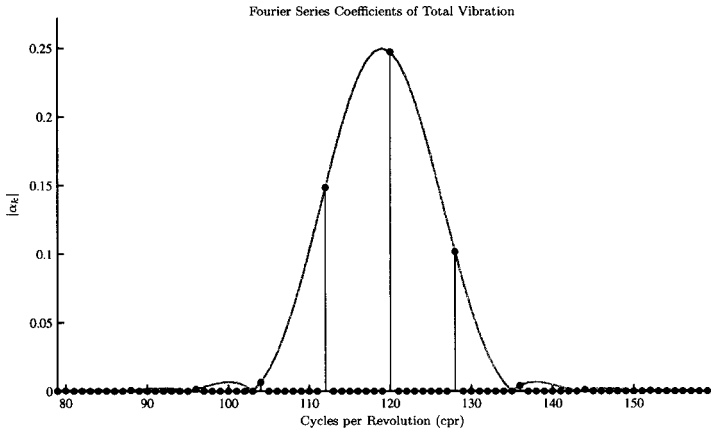

Fig. 1 The stem plot shows the amplitude of continuous-time Fourier series (CTFS) coefficients for the total vibration. The solid curve represents the CTFS coefficients for a single planet multiplied by *P*.

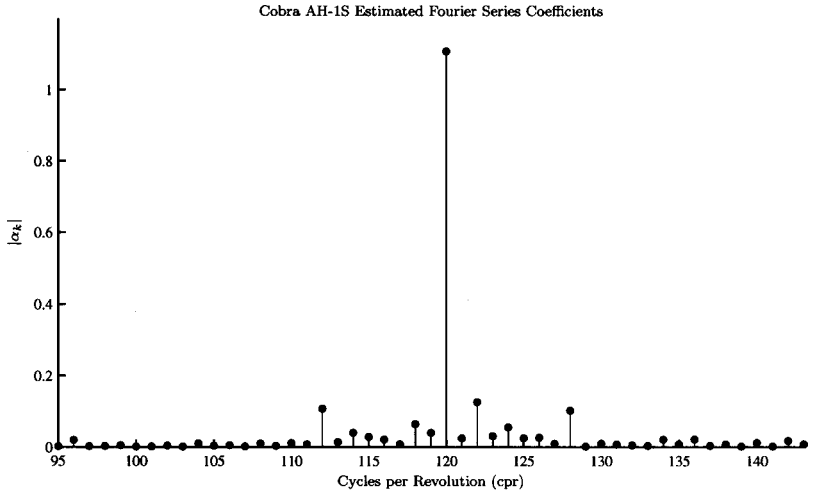

Fig. 2 DFT approximation of continuous-time Fourier series coefficients for the first harmonic of a vibration signal recorded from the upper planetary system of a Cobra AH-1S helicopter gearbox

$$v(r) = P \sum_{k=-\infty}^{\infty} a_{1,kP} e^{j2\pi kPr}. \quad (4)$$

This indicates that the CTFS representation of the total vibration is proportional to the CTFS representation of a single planet gear sampled at frequencies that are multiples of P, $\alpha_k = P a_{1,kP}$.

3 Asymmetrical Sidebands

Figure 1 shows the CTFS coefficients of a single, simulated planet gear from the upper planetary system of a Cobra AH-1S helicopter gearbox multiplied by P. This gearbox contains $P = 8$ planet gears and the annulus has $T = 119$ teeth. This figure also shows the simulated total vibration CTFS coefficients [Eq. (2)]. Note that they coincide exactly at frequencies that are multiples of $P = 8$, as predicted by Eq. (4), and the significant components only occur near the meshing frequency, $T = 119$ cpr.

The model developed here indicates that the cause of the asymmetry in the spectrum is due to the non-zero CTFS coefficients being misaligned with the meshing frequency. This misalignment will occur unless T is a multiple of P.

Figure 2 shows the DFT approximation of the CTFS coefficients near the first harmonic for a vibration signal recorded from a Cobra AH-1S gearbox. Synchronous averaging was used to eliminate noise that was asynchronous with the carrier frequency. The dominant components occurred at multiples of P near the meshing frequency (119 cpr), as predicted by the model.

Another significant consequence of the CTFS analysis is that it indicates the shape of spectrum near each of the meshing-frequency harmonics should vary, depending on how the non-zero coefficients are aligned.

4 Conclusions

This Tech Brief revisited the topic of epicyclic gearbox vibration analysis using continuous-time Fourier series (CTFS) analysis. This yielded insights about how the elasticity of the gearbox affects the shape of the spectrum as estimated by the CTFS coefficients. Specifically, this analysis explains the source of the asymmetry observed in the spectrum and correctly predicts the location of the dominant frequency components near all harmonics of the meshing frequency. This is especially important for health monitoring applications because it demonstrates that asymmetry occurs naturally and is not necessarily cause for alarm.

Acknowledgments

The author is grateful to Edward Huff, Eric Barszcz, Marianne Mosher, Mark Dzwonczyk, and the anonymous reviewers for their thoughtful review, assistance, and suggestions.

References

[1] Dousis, Dimitri A., 1992, "A Vibration Monitoring Acquisition and Diagnostic System for Helicopter Drive Train Bench Tests," *48th Annual Forum Proceedings of the American Helicopter Society*, Vol. 1, pp. 355–369.

[2] Ma, J., and Li, C. J., 1996, "Gear Defect Detection Through Model-Based Wideband Demodulation of Vibrations," Mech. Syst. Signal Process., **10**, No. 5, pp. 653–665.

[3] McFadden, P. D., and Smith, J. D., 1985, "An Explanation for the Asymmetry of the Modulation Sidebands About the Tooth Meshing Frequency in Epicyclic Gear Vibration," Proc. Inst. Mech. Eng., Part C: Mech. Eng. Sci., **199**, No. 1, pp. 65–70.

Theoretical and Experimental Analysis of Nonlinear Dynamics in a Linear Compressor

Gyu-Sang Choe
Graduate Student

Kwang-Joon Kim
Professor
e-mail: kjkim@mail.kaist.ac.kr

Center for Noise and Vibration Control,
Department of Mechanical Engineering, KAIST,
Science Town, Taejon 305-701, Korea

Steady-state nonlinear response characteristics of a linear compressor are investigated theoretically and experimentally. In the theoretical approach, motions of not only piston but also cylinder are considered and dynamic models for steady-state response predictions are formulated by applying the describing function method. Effects of piston mass on the jump phenomena are predicted by the derived models as an example of design parameter variation and compared with actual experimental results.
[DOI: 10.1115/1.1424297]

Introduction

Linear oscillating motors are inherently more potential in energy efficiency than other types for light duty compressors. This is why research has focused on this topic for the past 30 years. The major concern in previous studies [1–6] was that system performance under stable operations and, system instability problems, which might arise in practice, were not well understood probably because of complexities in the dynamic modeling of the system.

Configuration of a linear compressor under study is simple: a circular cylinder fixed onto a stator is supported by ground springs and a piston fixed onto a moving magnet is suspended by piston springs. Piston movement, however, is determined in a rather complicated way by interaction of mechanical parts with electromagnetic and thermodynamic subsystems. The gas force in compression chamber possesses inherently nonlinear characteristics with respect to the piston motion and, hence, its dynamic components are coupled to static components. Furthermore, motion of the piston is not mechanically constrained. Therefore, piston motion becomes uncontrollable under some operating conditions.

Choe and Kim [7] derived a dynamic model for a linear compressor and necessary conditions for the jump motion of the piston to occur by employing the describing function approach under the assumption that the cylinder was fixed to the earth. In reality, however, the cylinder moves by interacting with the piston; this is taken into account for more accuracy and, so, the effects of piston mass as a design parameter on the jump phenomena are analyzed based on the derived model and compared with actual experimental results.

Dynamic Modeling of Linear Compressor System

The mechanical subsystem is treated as a two-degree of freedom (DOF) model as shown in Fig. 1, where $u_1(t)$ and $u_2(t)$ denote respectively displacements of the piston m and the cylinder m_c from the static equilibrium positions.

The motion of piston and cylinder can be described by the following equations:

$$m\frac{d^2u_1(t)}{dt^2}+c\left(\frac{du_1(t)}{dt}-\frac{du_2(t)}{dt}\right)+k(u_1(t)-u_2(t))+k(X_0-X_S)-f_g(t)=f_e(t) \tag{1}$$

$$m_c\frac{d^2u_2(t)}{dt^2}+c_I\frac{du_2(t)}{dt}+k_Iu_2(t)-c\left(\frac{du_1(t)}{dt}-\frac{du_2(t)}{dt}\right)-k(u_1(t)-u_2(t))-k(X_0-X_S)+f_g(t)=-f_e(t) \tag{2}$$

where $f_g(t)$ denotes gas force in the compression chamber and $f_e(t)$ the electromagnetic exciting force exerted by the linear motor. In the above equations, X_s denotes the position of the piston when $f_e(t)$ and $f_g(t)$ don't act on the piston and X_0 denoting the equilibrium position of the piston varies with the piston amplitude and load (suction and discharge pressure).

The gas force is given by the following equation:

$$f_g(t)=A_p(P_c(t)-P_s) \tag{3}$$

where A_p, $P_c(t)$, and P_s denote the cross sectional area of the piston, compression chamber pressure and suction pressure respectively. It is assumed that the gas behaves as an ideal gas in the compression cycle, that is, compression and expansion processes are described by polytropic processes as follows:

$$P_c(t)=P_S\left(\frac{X_1}{x(t)}\right)^n \quad \text{for compression process} \tag{4}$$

$$P_c(t)=P_S\left(\frac{X_4}{x(t)}\right)^n \quad \text{for expansion process} \tag{5}$$

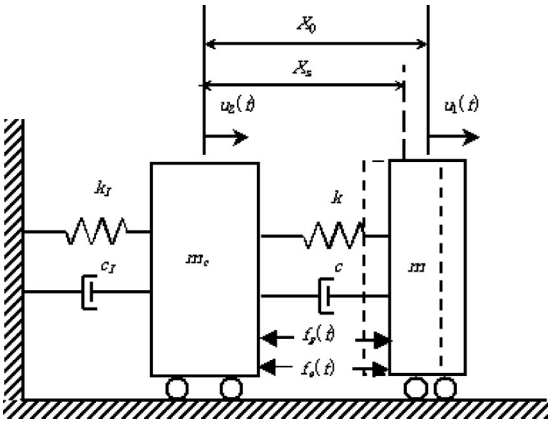

Fig. 1 A two-DOF model of mechanical subsystem

Contributed by the Technical Committee on Vibration and Sound for publication in the JOURNAL OF VIBRATION AND ACOUSTICS. Manuscript received Jan. 2000; Revised Aug. 2001. Associate Editor: A. F. Vakakis.

where n denotes the polytropic coefficient of the working gas and X_1 and X_4 are respectively final and initial positions of the piston relative to the discharge valve seat for suction process. The piston displacement $x(t)$ is given by

$$x(t)=X_0+u(t) \tag{6}$$

where $u(t)$ is the dynamic component of piston displacement defined by $u(t)=u_1(t)-u_2(t)$ and its amplitude is U.

Applying the describing function method [8] to the gas force and introducing a non-dimensional piston amplitude defined by $r_u=U/X_0$ yields the following expressions:

$$X_0=X_S+\frac{f_S(r_u)}{k} \tag{7}$$

$$U=\left(X_S+\frac{f_S(r_u)}{k}\right)r_u \tag{8}$$

$$F_e=(k+k_{eq}(r_u)-\omega^2M_{eq}+j\omega c+jh_{eq}(r_u))\left(X_S+\frac{f_S(r_u)}{k}\right)r_u \tag{9}$$

where F_e represents complex amplitude of the electromagnetic excitation force $f_e(t)$ and

$$f_S(r_u)=\frac{A_PP_S}{2\pi}\left(\int_0^{\theta_2}\left(\frac{1+r_u}{1+r_u\cos\theta}\right)^n d\theta+r_P(\pi-\theta_2)+\int_\pi^{\theta_4}\left(\frac{1+r_u\cos\theta_4}{1+r_u\cos\theta}\right)^n d\theta-\theta_4\right) \tag{10}$$

$$k_{eq}(r_u)=\frac{nA_PP_S}{\pi X_0}\left(\int_0^{\theta_2}\frac{(1+r_u)^n\sin^2\theta}{(1+r_u\cos\theta)^{n+1}}d\theta+\int_\pi^{\theta_4}\frac{(1+r_u\cos\theta_4)^n\sin^2\theta}{(1+r_u\cos\theta)^{n+1}}d\theta\right) \tag{11}$$

$$h_{eq}(r_u)=\frac{nA_PP_S}{(n-1)\pi r_uX_0}(r_p(\cos\theta_2+1)+\cos\theta_4-1) \tag{12}$$

$$M_{eq}=\left(\frac{k_I-\omega^2m_c+j\omega c_I}{k_I-\omega^2(m_c+m)+j\omega c_I}\right)m \tag{13}$$

In the above equations, $r_p=P_d/P_s$ is the nondimensional discharge pressure, θ denotes the coordinate of the piston in angular scale, and θ_2 and θ_4 represent the starting positions of discharge and suction respectively.

The electromagnetic exciting force in frequency domain F_e can be described as follows [9]:

$$F_e=\alpha I \tag{14}$$

where I is the complex amplitude of the current in the field coil and the proportional constant α is defined as the spatial derivative of the flux in the direction of the piston movement. Substituting Eq. (14) into (9) yields the current amplitude also as a function of the nondimensional piston amplitude r_u:

$$I=\frac{1}{\alpha}(k+k_{eq}(r_u)-\omega^2M_{eq}+j\omega c+jh_{eq}(r_u))\left(X_S+\frac{f_S(r_u)}{k}\right)r_u \tag{15}$$

The governing equation for the electro-mechanical circuit of a linear motor can be expressed in the time domain as follows [9]:

$$\alpha\frac{du(t)}{dt}+L_E\frac{di(t)}{dt}+R_Ei(t)=v(t) \tag{16}$$

where $v(t)$ is the input voltage, and L_E and R_E are effective inductance and resistance, respectively. The first term in Eq. (16) represents the electromotive force induced by the motion of the moving magnet. Transforming Eq. (16) into the frequency domain and substituting Eqs. (8) and (15) into this equation gives the relation between the voltage and the current in the frequency domain as follows:

$$V=\left(R_E+j\omega L_E+\frac{j\omega\alpha^2}{k+k_{eq}(r_u)-\omega^2M_{eq}+j\omega c+jh_{eq}(r_u)}\right)I \tag{17}$$

In summary, the equilibrium position of the piston, its amplitude, the current in the electric circuit, and required input voltage can be calculated without any difficulty for given values of the single dimensionless parameter r_u as shown in Eqs. (7), (8), (15) and (17) respectively, which makes a parametric study very easy although static and dynamic components are still coupled.

Theoretical and Experimental Analysis

Natural Frequency. Since the gas force behaves as a hardening spring at low amplitudes of the piston and a softening spring at high amplitudes, the natural frequency of the piston motion relative to the cylinder was expected to have such patterns. Figure 2 shows variations of the natural frequency with the nondimensional piston amplitude for three cases of nondimensional discharge pressure and a given piston mass ($m=0.534$ kg). Noting that the current in the coil is minimized when the driving frequency coincides with the natural frequency, consumption of the electric energy can be minimized by adjusting the driving frequency so that it may match well with the load and the required stroke.

Jump Phenomena. Jump phenomenon may arise due to the nonlinear spring characteristics of the gas force depending on the combination of mechanical, thermodynamic, and electromagnetic parameters (Choe and Kim [7]). Steady state responses for three piston masses are shown in Fig. 3. Theoretical results represented by solid lines in the figure show typical tangent bifurcation (Nayfeh and Balachandran [10]) for the two piston masses $m=0.534$ kg and 0.433 kg. The tangent bifurcation points denoted by solid circles in the figures are defined by $dr_u/dV=0$. Experimental results are represented in the figure by stars for increase of the input voltage and solid squares for decrease. The input voltages, at which the bifurcation was observed in Figs. 3(a) and (c), are about 30 percent greater than the predictions. This discrepancy might have been caused by many assumptions, examples of which would be the harmonic motion of the piston and the ideal behavior of the gas compression cycle. When the piston mass m was 0.467 kg, a value between two values, i.e., 0.534 kg and 0.433 kg, jump phenomenon was not observed in the experiment as well as in the prediction as shown in Fig. 3(b). This means that the jump phenomenon can be avoided just by selecting the piston mass in an optimum manner.

Influence of the Cylinder Motion. A real part of the effective mass of the moving piston M_{eq} calculated by Eq. (13) which takes into consideration the cylinder mass of 5.637 kg and cylinder mounting stiffness of 2.9 kN/m in this study is 0.431 kg while the piston mass by itself is 0.467 kg. Theoretical results for the

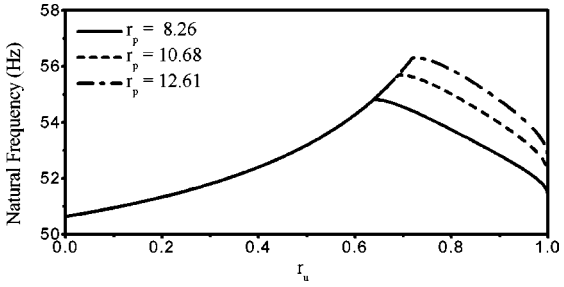

Fig. 2 Variations of piston natural frequency with amplitude

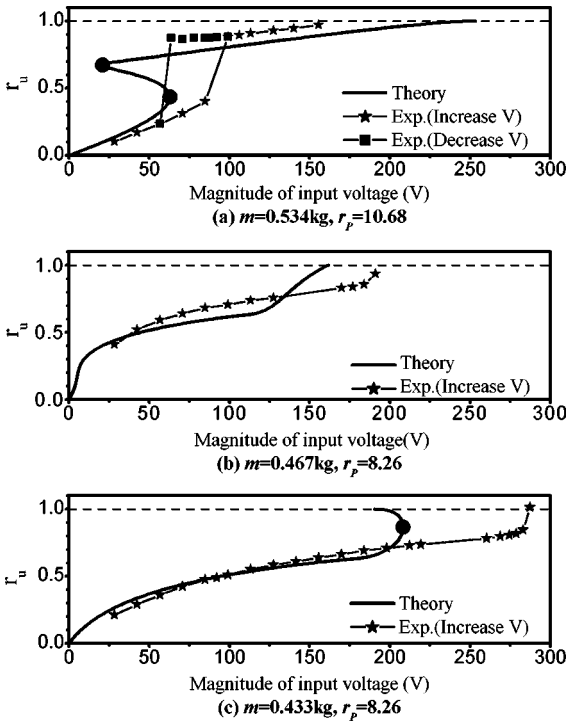

Fig. 3 Steady state nondimensional piston amplitudes versus input voltage

piston mass of 0.433 kg without considering the cylinder motion were close to Fig. 3(b) where no jump phenomenon is expected while jump arises in reality as shown in Fig. 3(c), meaning that inclusion of dynamics of the cylinder is crucial for the accurate stability analysis of the compressor system.

Concluding Remarks

A dynamic model of a linear compressor including motions of not only piston but also cylinder has been developed for analysis of its dynamic characteristics at the initial design stage. One important result is that variations of the natural frequency of the piston motion due to design parameter changes can be predicted by introducing the nondimensional piston stroke, which will also be useful to decide the driving frequency for enhancement of the system performance. Another important result is that the proposed model is capable of characterizing the nonlinear system behavior relatively well so that input voltage can be controlled in an optimum manner although the difference between the predicted input voltage for the tangent bifurcation and the measured is not negligible.

References

[1] Cadman, R. V., 1967, "A Technique for the Design of Electrodynamic Oscillating Compressors," Ph.D. thesis, Purdue University.

[2] Pollak, E., Soedel, W., Friedlaender, F. J., and Cohen, R., 1978, "Mathematical Model of an Electrodynamic Oscillating Refrigeration Compressor," *Proceedings of the Purdue Compressor Technology Conference*, pp. 246–259.

[3] Polman, J., De Jonge, A. K., and Castelijns, A., 1978, "Free Piston Electrodynamic Gas Compressor," *Proceedings of the Purdue Compressor Technology Conference*, pp. 241–245.

[4] Van der Walt, N. R., and Unger, R., 1992, "The Simulation and Design of a High Efficiency, Lubricant Free, Linear Compressor for a Domestic Refrigerator," *Proceedings of the International Compressor Engineering Conference at Purdue*, pp. 1–9.

[5] Minas, C., 1994, "Nonlinear Dynamics of an Oilless Linear Drive Reciprocating Compressor," ASME J. Vibr. Acoust., **116**, pp. 79–84.

[6] Choe, G. S., and Kim, K. J., 1997, "Linear Modeling of the Dynamics of an Electrodynamic Piston Compressor," *Proceedings of the 5th International Congress on Sound and Vibration*, Adelaide, Australia, pp. 1829–1836.

[7] Choe, G. S., and Kim, K. J., 2000, "Analysis of Nonlinear Dynamics in a Linear Compressor," JSME Int. J., Ser. C, **43**, pp. 545–552.

[8] Slotine, J. E., and Li, W., 1991, *Applied Nonlinear Control*, Prentice-Hall.

[9] Nasar, S. A., and Boldea, I., 1987, *Linear Electric Motors: Theory, Design, and Practical Applications*, Prentice-Hall.

[10] Nayfeh, A. H., and Balachandran, B., 1995, *Applied Nonlinear Dynamics*, John Wiley & Sons, Inc.

Robust Feedback Control of a Baffled Plate via Open-Loop Optimization

P. De Man
Graduate Student

A. François
Graduate Student

A. Preumont
Professor, Mem. ASME
e-mail: andre.preumont@ulb.ac.be

Active Structures Laboratory,
Université Libre de Bruxelles,
CP. 165-42, 50 Av. F.D. Roosevelt,
B-1050 Brussels, Belgium

A SISO control system is built by using a volume displacement sensor and a set of actuators driven in parallel with a single amplifier. The actuators location is optimized to achieve an open-loop transfer function which exhibits alternating poles and zeros, as for systems with collocated actuators and sensors; the search procedure uses a genetic algorithm. The ability of a simple lead compensator to control this SISO system is numerically demonstrated. [DOI: 10.1115/1.1421610]

1 Introduction

According to the modern control theory [1], an arbitrary control problem is mathematically formulated as the minimization of some norm of the closed-loop transfer function between the disturbance w and the performance metric z (Fig. 1):

$$T_{zw}=G_{zw}+G_{zu}H(I-G_{yu}H)^{-1}G_{yw} \tag{1}$$

where G_{zw} is the open-loop transfer function between the disturbance w and the performance metric z, G_{zu} between the control input u and the performance metric z, and G_{yw} between the disturbance w and the output measurement y, and G_{yu} between the control input u and the system output y.

This abstract formulation, although mathematically attractive, does not explicitly take into account the particular features of the problem considered; in particular, for structural acoustics, the small stability margin of the plant, or its large modal density and large (in fact infinite) dimensionality.

For the problem considered in this study, the performance objective is to minimize the far field radiated noise power, which cannot be used directly for feedback and requires the application of radiation filters which reconstruct the radiated noise power from the modal information of the vibrating structure [2]. Radiation filters were first used in control design by Baumann et al. [3]; they were used in a LQG framework [4,5], and using H_∞ and

Contributed by the Technical Committee on Vibration and Sound for publication in the JOURNAL OF VIBRATION AND ACOUSTICS. Manuscript received Aug. 2000; Revised Aug. 2001; Associate Editor: R. L. Clark.

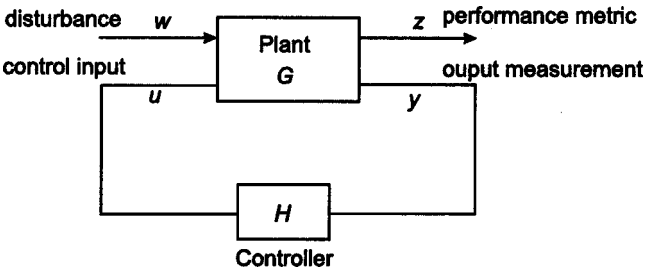

Fig. 1 Block diagram of the control structure

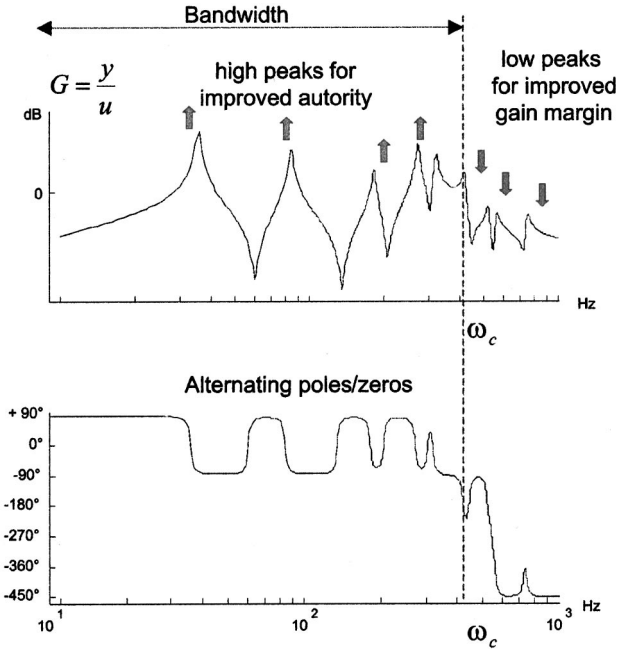

Fig. 2 Desired features of the open-loop FRF

μ-synthesis [6]. Snyder et al. [7] used optimally shaped piezopolymer (PVDF) films to measure transformed modes in order to reconstruct structural radiation. At low frequency, the asymmetric modes with zero net volume velocity radiate poorly in the far field and the odd-odd modes are the dominant radiators; there is a strong correlation between the radiated sound power and the volume velocity (in fact, asymptotically, as $\omega \rightarrow 0$, the first radiation mode as defined by Cunefare [2] or by Elliott and Johnson [8] is proportional to the volume velocity). This brought the idea of developing volume velocity (or volume displacement) sensors which would allow to identify the single output measurement to the scalar performance metric. Identifying y and z in Eq. (1) brings substantial simplifications: $G_{zu}=G_{yu}$, $G_{zw}=G_{yw}$, and

$$T_{zw}=T_{yw}=(I-G_{yu}H)^{-1}G_{yw} \tag{2}$$

with the additional benefit of dealing with a single output (SO) system. Various volume velocity or displacement sensors have been proposed [9–12]. The volume displacement is assumed to be available in this study.

For lightly damped vibrating structures, the open-loop system plays a role far more important than Eq. (2) suggests and the structure of G_{yu} depends critically on the type and location of the actuators and sensors.

The Hankel singular values are often used as optimization criterion for actuator and sensor placement [13]; the method has been adapted to disturbance rejection [14], to spillover alleviation [15] and mode targeting [16], with various numerical applications [17–19] and experiment [20]. These methods optimize the coupling of certain modes with candidate actuator/sensor locations, without paying attention to the pole/zero pattern of the open-loop system.

On the other hand, it is widely known that collocated actuator/sensor pairs are highly advisable whenever possible, because they guarantee alternating poles and zeros; this key property is responsible for the robustness of the control system with respect to the parametric uncertainty [21] (such as, for example, a shift in the natural frequency of the plate).

In this paper, alternating poles and zeros, control authority and spillover are considered simultaneously in the optimization process. We consider the SISO transfer function G_{yu} between a set of actuators driven in parallel and a volume displacement sensor; the actuator location is optimized to provide the open-loop frequency response function (FRF) with the following desirable features illustrated in Fig. 2:

- Alternating poles and zeros are sought within the control bandwidth to enhance the immunity with respect to the parametric uncertainty and to allow low order controllers.
- The magnitude of the resonance peaks is maximized within the control bandwidth to increase the control authority.
- The magnitude of the resonance peaks is minimized near and right after the cross-over frequency to improve the gain margin and reduce spillover.

2 Optimization

The actuator placement optimization uses a genetic algorithm (our implementation of the genetic algorithm uses the MATLAB toolbox GAOT [22]). The challenge is to formulate a fitness (cost) function which is easy to calculate and, at the same time, reflects the physical requirements of the open-loop FRF (Fig. 2). The modal expansion of the FRF between a single actuator and the volume displacement sensor takes the classical form

$$G(\omega)=\sum_{i=1}^{\infty}\frac{\phi_i(a)V_i}{\mu_i(\omega_i^2-\omega^2+2j\xi_i\omega\omega_i)} \tag{3}$$

where μ_i, ω_i and ξ_i are the modal mass, the natural frequency and the modal damping of mode i, V_i is the modal volume displacement and $\phi_i(a)$ is the modal amplitude (displacement) at the actuator location. In case of several actuators acting in parallel with a single power source, $\phi_i(a)$ is simply the sum of modal amplitudes at the actuators location.

The alternating poles/zeros requirement can be expressed by using an interesting property of undamped SISO structural systems: *if two neighboring modes are such that their residues have the same sign in the modal expansion of the open-loop FRF, there is always an imaginary zero between them* [23]. We thus define the following fitness function to be maximized:

$$F_1=\sum_i \text{sign}[\phi_i(a)V_i] \tag{4}$$

where $\text{sign}(.)=1,0,-1$ according to the sign of the argument. The sum over i extends to all the modes belonging to the frequency band where alternating poles and zeros are sought. Clearly, maximizing F_1 is equivalent to enforcing positive residues in the modal expansion (Eq. 3).

Next, the good controllability of the modes within the bandwidth calls for a large modal amplitude at the actuator for all the modes within the controller bandwidth. This can be enforced by defining the second contribution to the fitness function:

$$F_2=\sum_i \alpha_i|\phi_i(a)| \tag{5}$$

where α_i are weighting factors. Finally, in order to minimize the controllability in the cross-over region and slightly beyond, the following contribution can be added:

$$F_3 = -\sum_j \beta_j |\phi_j(a)| \tag{6}$$

this term is negative because the fitness function is maximized; β_i are also weighting factors. The global fitness function is

$$F = F_1 + F_2 + F_3 \tag{7}$$

Notice that the above fitness function is straightforward to compute from the knowledge of the mode shapes only; this property is essential to speed up the optimization process. Note also that the limit between the modes contributing to the various contributions of the fitness function is flexible; some of the modes near cross-over may be included in F_1 to guarantee alternating poles and zeros (in order to achieve phase stabilization), but also in F_3, to minimize their impact on the open-loop FRF. The coefficients α_i and β_i are free parameters which can be used for shaping the open-loop transfer function.

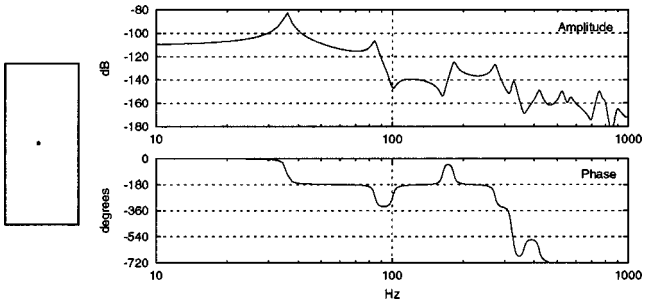

Fig. 3 Open-loop FRF with arbitrary actuator location

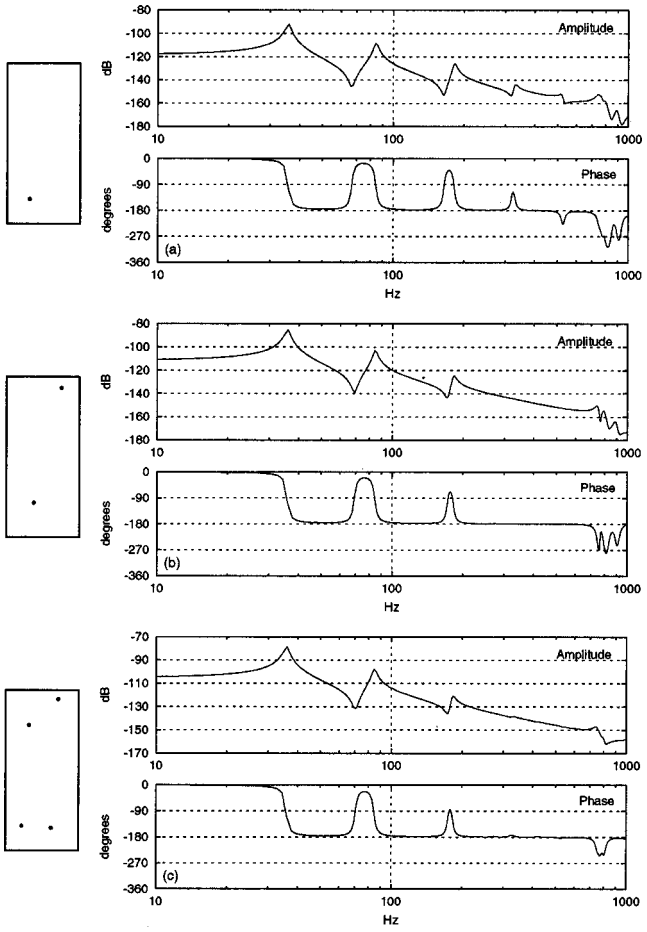

Fig. 4 Open-loop FRF and optimum actuator locations for 1, 2 and 4 point force actuators

3 Application

The proposed strategy has been applied numerically to a glass plate [24]. The bandwidth has been chosen close to 250 Hz to include three modes contributing to the volume velocity. Figure 3 shows the open-loop FRF for a single point force actuator arbitrarily located. Figure 4 shows the open-loop FRF after optimization and the optimal actuator locations. The results are discussed more extensively in [24] where piezoceramic actuators are also considered.

Open-loop control systems with FRF like those of Fig. 4 are easy to control. To illustrate this, the loop has been closed with a lead compensator, the parameters of which have been tuned to achieve a 10 dB gain margin and 65 deg phase margin. The FRF between the disturbance and the volume displacement, and the radiated sound power are compared in Fig. 5 for the case of 4 point force actuators. Figure 6 shows the 1/3 octave attenuation in dB.

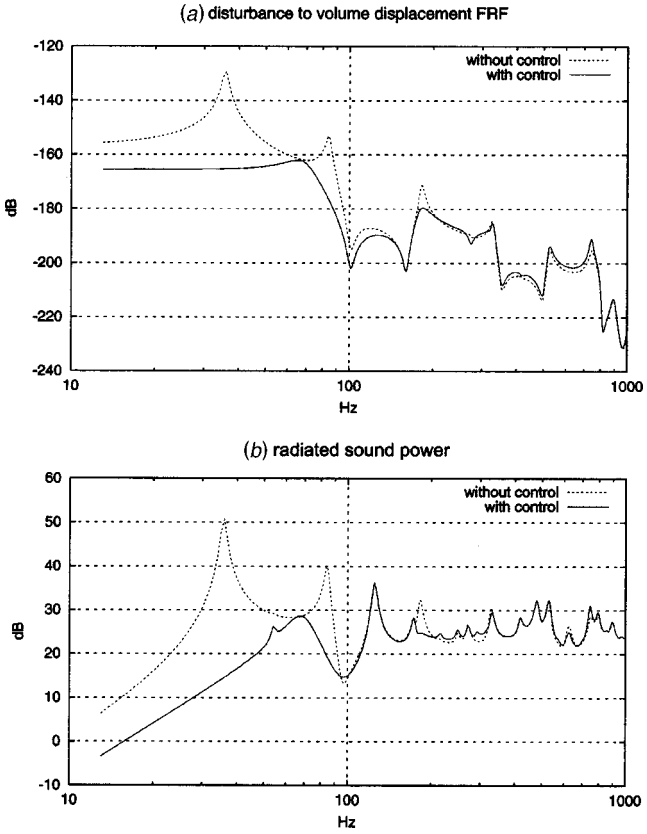

Fig. 5 Effect of a lead compensator (4 point force actuators)

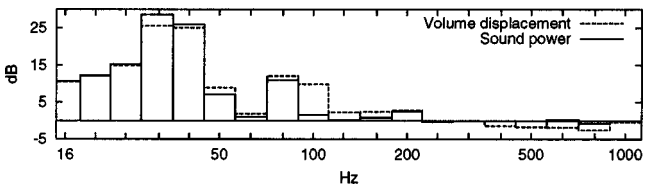

Fig. 6 1/3-octave reduction (in dB). 4 point force actuators.

4 Conclusions

This paper has addressed the actuator placement for a baffled plate with three simultaneous objectives: (i) enhance the immunity with respect to parametric uncertainty and allowing low order controllers by enforcing alternating poles and zeros within the bandwidth, (ii) maximize the control authority and (iii) reduce spillover. A very simple fitness function has been formulated which makes the genetic algorithm very effective. Finally, the interest of this control architecture is confirmed by closing the feedback loop with a lead compensator.

Acknowledgment

This work was supported by the Inter University Attraction Pole IUAP-IV-24 on Intelligent Mechatronics Systems and by the Ministry of *Région Wallonne* (DGTRE) under grants No. 3512 and No. 3363 (FIRST).

References

[1] Doyle, J. C., Francis, B. A., and Tannenbaum, R., 1992, *Feedback Control Theory*, Macmillan, New York.

[2] Cunefare, K. A., 1991, "The Minimum Multimodal Radiation Efficiency of Baffled Finite Beams," J. Acoust. Soc. Am., **90**, pp. 2521–2529.

[3] Baumann, W. T., Saunders, W. R., and Robertshaw, H. R., 1991, "Active Suppression of Acoustic Radiation from Impulsively Excited Structures," J. Acoust. Soc. Am., **90**, 3202–3208.

[4] Dehandschutter, W., Henrioulle, K., Swevers, J., and Sas, P., 1997, "State-space Feedback Control of Sound Radiation Using Structural Sensors and Structural Control Inputs," *Proceedings ACTIVE 97*, Budapest, August 21–23, pp. 979–983.

[5] Vipperman, J. S., and Clark, R. L., 1999, "Multivariable Feedback Active Structural Acoustic Control using Adaptive Piezoelectric Sensoriactuators," J. Acoust. Soc. Am., **105**, pp. 219–225.

[6] Cox, D. E., Gibbs, G. P., Clark, R. L., and Vipperman, J. S., 1999, "Experimental Robust Control of Structural Acoustic Radiation," ASME J. Vibr. Acoust., **121**, pp. 433–439.

[7] Snyder, S. D., Tanaka, N., and Kikushima, Y., 1996, "The Use of Optimally Shaped Piezo-Electric Film Sensors in the Active Control of Free Field Structural Radiation, Part 2: Feedback Control," ASME J. Vibr. Acoust., **118**, pp. 112–121.

[8] Elliott, S. J., and Johnson, M. E., 1993, "Radiation Modes and the Active Control of Sound Power," J. Acoust. Soc. Am., **94**, pp. 2194–2201.

[9] Rex, J., and Elliott, S. J., 1992, "The QWSIS-A New Sensor for Structural Radiation Control," *Proceedings of MOVIC*, Yokohama, pp. 339–343.

[10] Charette, F., Berry, A., and Guigou, C., 1997, "Active Control of Sound Radiation from a Plate Using a Polyvinylidene Fluoride Volume Displacement Sensor," J. Acoust. Soc. Am., **103**, pp. 1493–1503.

[11] Preumont, A., François, A., and Dubru, S., 1999, "Piezoelectric Array Sensing for Real-Time, Broad-Band Sound Radiation Measurement," ASME J. Vibr. Acoust., **121**, pp. 446–452.

[12] François, A., De Man, P., and Preumont, A., 2001, "Piezoelectric Array Sensing of Volume Displacement: A Hardware Demonstration," J. Sound Vib., **244**, pp. 395–405.

[13] Lim, K. B., and Gawronski, W., 1996, "Hankel Singular Values of Flexible Structures in Discrete Time," J. Guid. Control Dyn., **19**, pp. 1370–1377.

[14] Lim, K. B., 1997, "Disturbance Rejection Approach to Actuator and Sensor Placement," J. Guid. Control Dyn., **20**, pp. 202–204.

[15] Clark, R. L., and Cox, D. E., 1999, "Band-Limited Actuator and Sensor Selection for Disturbance Rejection," J. Guid. Control Dyn., **22**, pp. 740–743.

[16] Smith, G. C., and Clark, R. L., 1999, "Adaptive Structure Design Through Optimum Spatial Compensation," *Proceedings of Active 99*, Fort Lauderdale, FL, December 2–4.

[17] Lim, K. B., Lake, R. C., and Heeg, J., 1998, "Effective Selection of Piezoceramic Actuators for an Experimental Flexible Wing," J. Guid. Control Dyn., **21**, pp. 704–709.

[18] Clark, R. L., 1999, "Adaptive Structure: Compensators by Design," *Proceedings of Active 99*, Fort Lauderdale, FL, December 2–4.

[19] Rule, J. A., Richard, R. E., and Clark, R. L., 1999, "Design of an Aeroelastic Delta Wing Model for Active Flutter Control," *Proceedings of Active 99*, Fort Lauderdale, FL, December 2–4.

[20] Clark, R. L., and Cox, D. E., 1999, "Experimental Demonstration of a Band-Limited Actuator and Sensor Selection Strategy for Structural Acoustic Control," J. Acoust. Soc. Am., **106**, pp. 3407–3414.

[21] Preumont, A., 1997, *Vibration Control of Active Structures, An Introduction*, Kluwer, Dordrecht.

[22] Houck, C. R., Joines, J. A., and Kay, M. G., 1995, *A Genetic Algorithm for Function Optimization: A Matlab Implementation*, Technical Report 96-01, NCSU-IE.

[23] Martin, G. D., 1978, "*On the Control of Flexible Mechanical Systems*," Master's thesis, Stanford University.

[24] De Man, P., François, A., and Preumont, A., 2001, "Robust Feedback Control of a Baffled Plate Through Vibroacoustic Optimization," *42nd AIAA Structural Dynamics Conference in Seattle* April 16–19.

On the Proper Orthogonal Modes and Normal Modes of Continuous Vibration Systems

B. F. Feeny
Department of Mechanical Engineering,
Michigan State University,
East Lansing, MI 48824

1 Introduction

Proper orthogonal decomposition (POD) is a useful experimental tool in dynamics and vibration. A common application of POD to structures involves sensed displacements, $x_1(t)$, $x_2(t)$, . . . ,$x_M(t)$, at M locations on the structure. When the displacements are sampled N times at a fixed sampling rate, we can form displacement-history arrays, such that $\mathbf{x}_i=(x_i(t_1), x_i(t_2), \ldots, x_i(t_N))^T$, for $i=1, \ldots, M$. The mean values are often subtracted from the displacement histories. These displacement histories are used to form an $N\times M$ ensemble matrix,

$$\mathbf{X}=[\mathbf{x}_1, \mathbf{x}_2, \ldots, \mathbf{x}_M].$$

The $M\times M$ correlation matrix is $\mathbf{R}=1/N\mathbf{X}^T\mathbf{X}$. Since $\mathbf{R}$ is real and symmetric, its eigenvectors form an orthogonal basis. The eigenvectors and eigenvalues of $\mathbf{R}$ are the proper orthogonal modes (POMs) and values (POVs).

The POMs in certain nonlinear structures have resembled the normal modes of the linearized system [1–3]. The POMs may indeed converge to linear normal modes in multimodal free responses of symmetric lightly damped lumped-mass linear systems, but *only* if the mass matrix has the form $m\mathbf{I}$, which can be achieved by a coordinate transformation if the mass distribution is known [4]. This provides a fundamental tie between the statistically derived POMs and the geometrically based linear normal modes in certain discrete systems. In this note, this relationship is extended to discretized continuous systems.

2 Distributed-Parameter Linear Systems

The following analysis relates the POMs to the normal modes in continuous systems with discrete measurements and known mass.

2.1 Analysis of POD for Modal Responses. We consider a one-dimensional self-adjoint distributed-parameter system of length l:

$$m(x)\frac{\partial^2 y}{\partial t^2}+L_1 y=0, \tag{1}$$

with boundary conditions, where $y(x,t)$ is a displacement. Letting $u=m^{1/2}(x)y$, the system can be rewritten as

$$\frac{\partial^2 u}{\partial t^2}+L_2 u=0. \tag{2}$$

$L_2=m^{-1/2}(x)L_1 m^{-1/2}(x)$ is self-adjoint. Separation of variables leads to normalized eigenvalues and eigenfunctions $\phi_i(x)$ that satisfy

$$\int_0^L \phi_i(x)\phi_j(x)dx=\delta_{ij}.$$

Contributed by the Technical Committee on Vibration and Sound for publication in the JOURNAL OF VIBRATION AND ACOUSTICS. Manuscript received Feb. 1999; revised Aug. 2001. Associate Editor: A. F. Vakakis.

Sampling the displacement $u(x,t)$ at coordinates $x_1, \ldots, x_M$, leads to a set of measurements $\mathbf{u}=[u(x_1,t) \ldots u(x_M,t)]^T$. The displacement is approximated as a truncated series of linear normal modes, such that $u(x,t) \approx \Sigma_{i=1}^{\hat{M}} q_i(t)\phi_i(x) = \phi^T \mathbf{q}$, where $\phi = [\phi_1(x) \ldots \phi_{\hat{M}}(x)]^T$ is a vector of modal functions, and $\mathbf{q}(t) = [q_1(t) \ldots q_{\hat{M}}(t)]^T$ is the vector of modal coordinates. We will take $\hat{M}=M$. We define a matrix $\mathbf{\Phi}=[\mathbf{v}_1 \ldots \mathbf{v}_M] = [\phi(x_1) \ldots \phi(x_M)]^T$. Thus, the vectors $\mathbf{v}_i = [\phi_i(x_1) \ldots \phi_i(x_M)]^T$ are spatial discretizations of the mode shapes $\phi_i(x)$. Then

$$\mathbf{u}=\mathbf{\Phi}q(t)$$

relates the discrete displacements of the beam to the discretizations of the mode shapes.

The displacements are sampled at times $t_i = i\Delta t$, $i=1, \ldots, N$, where Δt is the sampling rate. We construct an $N \times M$ ensemble matrix $\mathbf{U}=[\mathbf{u}(t_1) \ldots \mathbf{u}(t_N)]^T = [\mathbf{\Phi q}(t_1) \ldots \mathbf{\Phi q}(t_N)]^T$, or

$$\mathbf{U}=(\mathbf{\Phi Q})^T,$$

where $\mathbf{Q}=[\mathbf{q}(t_1) \ldots \mathbf{q}(t_N)]$ is an $M \times N$ matrix. The correlation matrix is thus $\mathbf{R}=1/N\mathbf{U}^T\mathbf{U}=1/N\mathbf{\Phi Q Q}^T\mathbf{\Phi}^T$.

We check whether $\mathbf{v}_j$ is an eigenvector of $\mathbf{R}$ by examining $\mathbf{R v}_j = 1/N\mathbf{\Phi Q Q}^T\mathbf{\Phi}^T\mathbf{v}_j$. The quantity $\mathbf{\Phi}^T\mathbf{v}_j$ has elements $\mathbf{v}_i^T\mathbf{v}_j$. If the spatial discretization is *evenly spaced*, then, $\mathbf{v}_i^T\mathbf{v}_j = \Sigma_{k=1}^{M}\phi_i(x_k)\phi_j(x_k) \approx (1/h)\int_0^L \phi_i(x)\phi_j(x)dx$ by the rectangular rule, where h is the spacing of the spatial discretization. Thus we approximate $\mathbf{v}_i^T\mathbf{v}_j \approx (1/h)\delta_{ij}$. If this approximation is reasonable, then the quantity $\mathbf{\Phi}^T\mathbf{v}_j \approx [0 \ldots 0,1/h,0 \ldots 0]^T = \mathbf{h}_j$ has elements of approximately zero, except the jth element which is approximately $1/h$. The error associated with the rectangular integration representation of the underlying orthogonality integral is on the order of kh^2, where k is proportional to a characteristic curvature in the integrand [5]. Then $\mathbf{R v}_j \approx 1/N\mathbf{\Phi Q Q}^T\mathbf{h}_j$. The ijth elements of $\mathbf{QQ}^T$ are $\Sigma_{k=1}^{N} q_i(t_k)q_j(t_k)$. If the frequencies of oscillation of $q_i(t)$ and $q_j(t)$ are distinct, the sampling rate is Δt is fixed, and the time record gets arbitrarily large, then

$$\lim_{N\to\infty} \frac{1}{N}\sum_{k=1}^{N} q_i(t_k)q_j(t_k)=0, \quad i \neq j.$$

Thus,

$$\lim_{N\to\infty} \frac{1}{N}\mathbf{QQ}^T=\mathbf{D}$$

which is diagonal with elements $d_{ii}=\Sigma_{k=1}^{N} q_i(t_k)^2/N$, which are the mean squared values of $q_i(t)$.

In such case, $\mathbf{R v}_j \to 1/N\mathbf{\Phi D\Phi}^T\mathbf{v}_j \approx \mathbf{\Phi D h}_j = \mathbf{\Phi h}_j d_{jj} = \mathbf{v}_j d_{jj}/h$. So, for increasing N, with a fixed sampling rate, evenly spaced sensors and distinct modal frequencies, the POMs converge approximately to $\mathbf{v}_j$, which are the discretized linear modes. (The POMs converge to $\mathbf{v}_j + \mathbf{e}_j$ where $\mathbf{e}_j$ is an error vector.) Furthermore, the POVs converge to d_{jj}/h, which is proportional to the mean squared modal coordinate.

Thus, we have an analysis which ties the statistically formulated POMs to the discretization of the nonlinear normal modes for multi-modal free responses of undamped systems with known mass distributions.

The role of the mass distribution is critical. The modes of Eq. (1) are orthogonal with respect to the mass distribution (and the linear operator), and are not otherwise perpendicular to each other. Discretized modes are therefore not perpendicular. The POMs, however, are orthogonal (i.e. perpendicular), since $\mathbf{R}^T=\mathbf{R}$. Thus, for general mass distributions, the POMs cannot represent the discretized linear normal modes. Formulating with respect to the mass, as in Eq. (2), allows us to make a connection between POMs and normal modes in multi-modal responses. The limitation is that the mass distribution must be uniform or known.

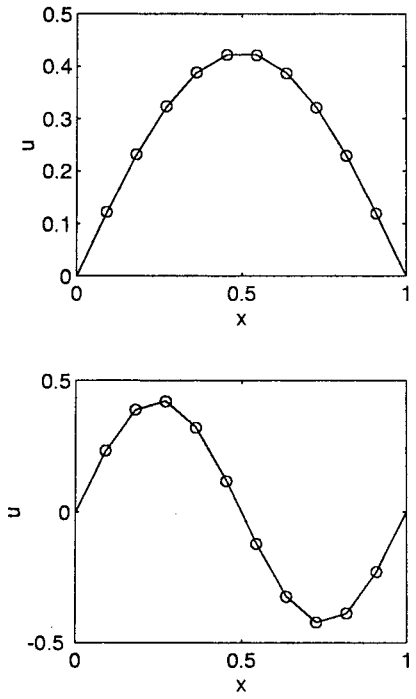

Fig. 1 The first two discretized linear normal modes of a hinged-hinged beam are plotted with a solid line. The corresponding POMs are plotted with circles.

2.2 Numerical Examples. We apply these ideas to a hinged-hinged beam, for which theoretical modes are readily available for comparison. For each numerical simulation, we choose a uniform mass per unit length of $m(x)=1$, a stiffness of $EI=1$, and a length of $L=1$. The clamp is at $x=0$.

In putting ten "sensors" on the beam away from the endpoints, the spacing was $h=1/11$. Here, the modal functions are $\phi_i(x) = \sin(i\pi x)$. The inner product between the discretized modal vectors was, to at least four decimal points, $\mathbf{v}_i^T\mathbf{v}_j = \delta_{ij}/h$. The modal frequencies, $\omega_i = i^2\pi^2$, are distinct and widely spaced.

Vibrations were induced through the modal variables; $\mathbf{q}(0) = [2,1,0.5,0.25,0.12,0.1,0.05,0.05,0.05,0.05]^T$ and $\dot{\mathbf{q}}(0)=\mathbf{0}$ were the initial conditions. The vibrations were sampled through four fundamental periods at an interval of $\Delta t = 0.0179$ (400 samples). Figure 1 shows the comparison between the first two sets of modes. The higher modes visually compared as well as those shown. The norms of the errors between the first four sets of modes are 0.0037, 0.0049, 0.0052 and 0.0055. The mean norm of the error between the ten computed modes is 0.0863.

A cantilevered beam model was similarly tested. This case is more sensitive to the spatial discretization effects [6]. The discretized modes are not orthogonal, with errors of about 20 percent among the first three modes. Figure 2 compares the first two sets of modes.

3 Synchronous Nonlinear Modes

Since the principal axes optimize the distribution of data from the axes, the dominant POM can be considered as an optimal fit of a "synchronous" nonlinear normal mode during a single-mode response [4] ("synchronous" meaning that the displacement coordinates reach their extrema simultaneously). As the amplitude of the response changes, the path of the synchronous normal mode changes, as does its best fit.

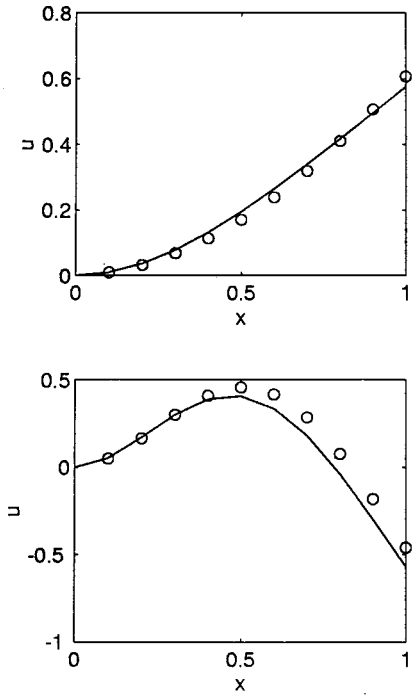

Fig. 2 The first two discretized linear normal modes of a cantilevered beam are plotted with a solid line. The corresponding POMs are plotted with circles.

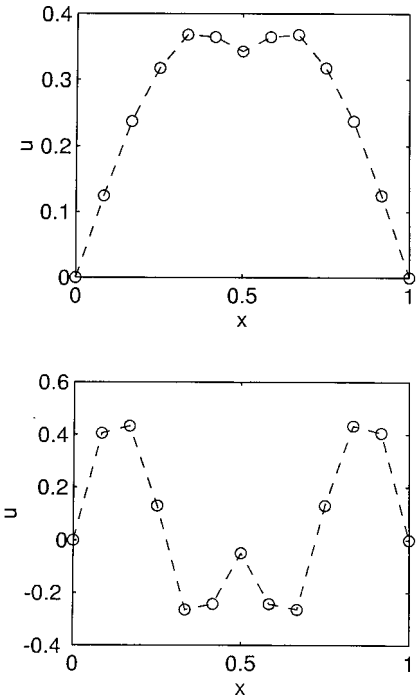

Fig. 4 The two most dominant POMs for a nonlinear beam vibrating in the first nonlinear normal mode. The dominant POM corresponds to 99.8 percent of the signal power.

This interpretation may extend to multi-modal nonlinear modal responses in some cases [7]. However, the relationship between the POMs and the ''best fit'' of the nonlinear normal modes is generally obscured if more than one mode is active.

3.1 Nonlinear Example. The equation of motion of a hinged beam with a discrete cubic spring at its midpoint [8] is

$$m\ddot{u}+EIu''''+u^3\delta(x-l)=0, \tag{3}$$

with $u(x,t)=u''(x,t)=0$ at $x=0$ and $x=L=2l$, where $u(x,t)$ is the deflection of the beam and δ is the Dirac delta function. The parameters are $m=EI=L=1$. Equation (3) can be discretized using the assumed-modes method [9]. If u is expanded in a truncated modal series as $\mu(x,t)=\Sigma_{i=1}^{M}q_i(t)\phi_i(x)$, where $\phi_i(x)=\sin(i\pi x/L)$, the resulting discretized equations of motion are $\ddot{\mathbf{q}}+\mathbf{\Lambda q}+\mathbf{f}(\mathbf{q})=\mathbf{0}$, where $\mathbf{\Lambda}$ is a diagonal matrix of natural frequencies squared, and $\mathbf{f}(\mathbf{q})$ has elements $f_i=u(l)^3\sin(i\pi/2)$.

The numerical solution (fifth-order Runge-Kutta) was based at initial conditions $\mathbf{q}(0)=[4.0000,0,0.2244,0,-0.2291,0,0.1023,0,-0.0561,0]^T$ and $\dot{\mathbf{q}}(0)=\mathbf{0}$, very nearly exciting only the first nonlinear normal mode. Three periods of motion in this nonlinear mode were sampled at a step size of $\Delta t=0.0255$ ($N=180$). Figure 3 shows the animated modal vibration and its shape variation with phase.

The displacements along the beam were obtained from the truncated modal expansion, and evaluated at $M+1$ evenly spaced locations along the beam. The redundant ''sensor'' was added so that the evenly spaced discretization included the midpoint of the beam. The three largest POVs were 46.9601, 0.1227, and 0.0003. Thus the dominant POM comprised about 99.8 percent of the mean signal power. The two dominant POMs are plotted in Fig. 4. The dominant POM of the discrete measurements qualitively fits the animated synchronous motion. Figure 5 plots the displacement of the midpoint of the beam against the displacement at location $x=l/6$. Superposed on this plot is a projection of the dominant POM onto this coordinate space. The POM is aligned with the principal axis of minimum moment of inertia of the data.

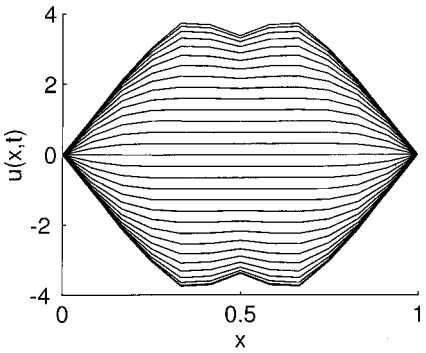

Fig. 3 An animation of vibration in the first nonlinear normal mode of a nonlinear beam

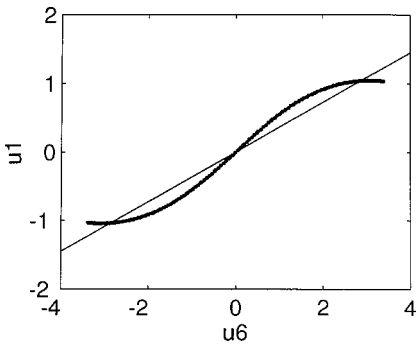

Fig. 5 The deflection $u_1(t)$ at $x=0.0825$ versus the deflection $u_6(t)$ at $x=0.5$ during vibration in the first nonlinear normal mode. The straight line is the projection of the dominant POM.

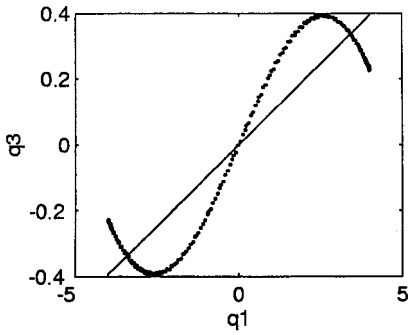

Fig. 6 The deflections of linear modal coordinate q_3, versus the first linear modal coordinate, q_1, of a nonlinear beam during vibration in the first nonlinear normal mode. The straight line is the projection of the dominant POM.

Figure 6 plots two modal coordinates against each other. This plot shows how the relative participation of each linear mode changed during the first nonlinear modal vibration. Superposed on the plot is the projection of the first POM computed from an ensemble of modal displacements. The dominant POM is a best fit of the synchronous normal mode, and not its linearization.

4 Conclusion

The POMs approximate the discretized linear normal modes for free multi-modal motions of distributed systems. The approximation depends on the sensors' spatial resolution. The problem must be formulated in displacement coordinates defined such that the associated mass distribution is uniform.

The dominant POM produces a best fit of a single active ''synchronous'' discretized nonlinear normal mode.

The results relate the statistically derived POMs and the geometry of normal modes, for multi-modal responses of a class of linear continuous systems, and also for single mode nonlinear responses.

Acknowledgment

This work was supported by the National Science Foundation (CMS-9624347).

References

[1] Cusumano, J. P., and Bai, B.-Y., 1993, ''Period-Infinity Periodic Motions, Chaos, and Spatial Coherence in a 10 Degree of Freedom Impact Oscillator,'' Chaos, Solitons Fractals, **3**, No. 5, pp. 515–535.

[2] Davies, M. A., and Moon, F. C., 1997, ''Solitons, Chaos, and Modal Interactions in Periodic Structures,'' *Nonlinear Dynamics: The Richard Rand 50th Anniversary Volume*, A. Guran, ed., World Scientific, Singapore, pp. 119–143.

[3] Kust, O., 1997, ''Modal Analysis of Long Torsional Strings Through Proper Orthogonal Decomposition,'' Zeitschrift für angewandte Mathematik und Mechanik, **77**, S1, pp. S183–S184.

[4] Feeny, B. F., and Kappagantu, R., 1998, ''On the Physical Interpretation of Proper Orthogonal Modes in Vibrations,'' J. Sound Vib., **211(4)**, pp. 607–616.

[5] Forsythe, G. E., Malcolm, M. A., and Moler, C. B., 1977, *Computer Methods for Mathematical Computations*, Prentice Hall, Englewood Cliffs.

[6] Feeny, B. F., and Liang, Y., 2001, ''Interpreting Proper Orthogonal Modes of Randomly Excited Linear Vibration Systems,'' submitted.

[7] Ma, X., Azeez, M. A. F., and Vakakis, A. F., 1998, ''Nonparametric Nonlinear System Identification of a Nonlinear Flexible System Using Proper Orthogonal Mode Decomposition,'' *Seventh Conference on Nonlinear Vibrations, Stability, and Dynamics of Structures*, Blacksburg, VA.

[8] Boivin, N., Pierre, C., and Shaw, S. W., 1995, ''Non-Linear Normal Modes, Invariance, and Modal Dynamics Approximations of Non-Linear Systems,'' Nonlinear Dyn., **8**, pp. 315–346.

[9] Meirovitch, L., 1997, *Principles and Techniques of Vibrations*, Prentice Hall, Upper Saddle River.